Advanced Functional Materials

ADVANCED FUNCTIONAL MATERIALS
www.afm-journal.de

RESEARCH ARTICLE OPEN ACCESS

Self-Assembled Hybrid Cell-Enzyme Materials for Gas-Powered Biocatalysis

Marius Stoeckle | Kersten S. Rabe | Christof M. Niemeyer

Institute for Biological Interfaces 1 (IBG1), Karlsruhe Institute of Technology (KIT), Eggenstein-Leopoldshafen, Germany

Correspondence: Christof M. Niemeyer (niemeyer@kit.edu)

Received: 9 June 2026 | **Revised:** 24 August 2026 | **Accepted:** 27 August 2026

Keywords: cofactor regeneration | enzyme networks | gas-powered biocatalysis | hybrid catalytic materials | metabolic integration | self-assembled materials

ABSTRACT

The integration of biological energy conversion into functional materials represents a key challenge in the development of advanced catalytic systems. Here, we introduce self-assembled cell-enzyme hybrid materials that integrate cellular metabolism with programmable enzyme networks for gas-powered biocatalysis. By harnessing the native formate hydrogenlyase machinery of *Escherichia coli*, H_2 and CO_2 are converted into formate, which serves as a transient electron carrier for enzymatic NADH regeneration by a highly stable formate dehydrogenase. Integration of a transhydrogenase further provides access to NADPH-dependent pathways, establishing a modular redox platform that can be coupled to diverse downstream biocatalysts. The catalytic system is translated into ready-to-use material formats through cryogenic fabrication of lyophilized carrier-free hybrid beads and their subsequent encapsulation into alginate composites, enabling simple "count-and-add" operation, catalyst recycling, and robust performance under challenging reaction conditions. By exploiting H_2 as the reducing substrate while recycling CO_2 within the formate-mediated regeneration cycle, the system avoids sacrificial organic reduction equivalents and associated by-products, resulting in high atom economy. The integration of metabolic energy conversion, programmable self-assembly, and materials engineering thus provides a general strategy for gas-powered redox biocatalysis.

1 | Introduction

The development of sustainable chemical processes increasingly relies on biocatalysis, where enzymes enable highly selective transformations under mild conditions [1–5]. However, a large fraction of industrially relevant reactions depends on reduced nicotinamide cofactors such as NADH and NADPH, whose continuous regeneration remains a central challenge for scalable implementation [6]. Conventional regeneration strategies typically rely on sacrificial organic substrates, resulting in reduced atom economy, accumulation of by-products, and limited process sustainability [7]. Alternative approaches based on electrochemical or hydrogenase-driven systems offer improved redox efficiency but often suffer from limited robustness, complex implementation, or restricted compatibility with standard production hosts [8–10].

Recent advances in biocatalysis have demonstrated that cascades of isolated enzymes enable efficient multistep transformations under mild conditions, but their practical implementation is often limited by cofactor supply, stability, and process integration. Embedding such catalytic systems into structured materials has emerged as a powerful strategy to overcome these limitations by improving enzyme stability, enhancing mass transport, and enabling cofactor retention under continuous operation [11–15]. In particular, carrier-free all-enzyme materials assembled via genetically encoded interaction modules have emerged as a versatile platform that combines high catalytic density with

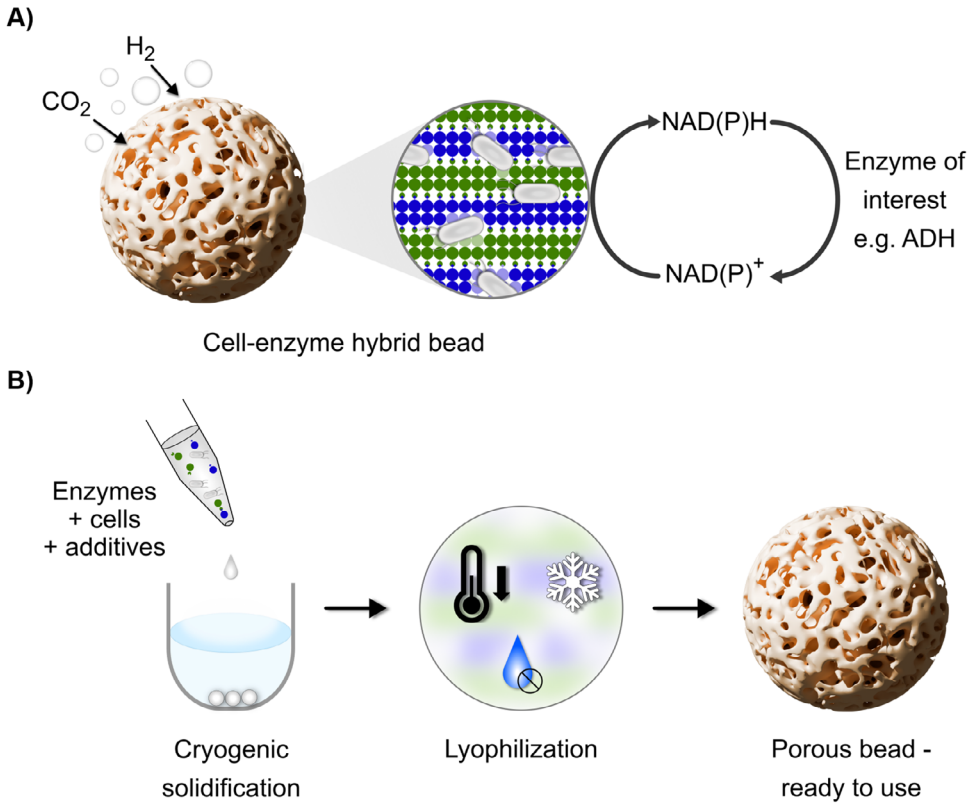

FIGURE 1 | Gas-powered hybrid catalytic materials integrating cellular metabolism and programmable enzyme networks. (A) Concept of a self-assembled catalytic bead in which gaseous substrates are converted by cells embedded in a carrier-free enzyme network to generate reducing equivalents (NADH/NADPH) within a single material entity. These cofactors can be directly harnessed to drive downstream biocatalytic transformations by coupled enzymes, exemplified here by alcohol dehydrogenases (ADH). The hybrid architecture enables spatial confinement, efficient mass transport, and functional integration of multiple catalytic processes. (B) Droplet-based fabrication strategy combining cells with complementary enzyme building blocks and stabilizing additives, followed by cryogenic solidification and lyophilization to yield monodisperse, ready-to-use hybrid beads.

programmable architecture [16]. Building on this concept, we have recently introduced monodisperse all-enzyme hydrogel beads as structurally defined, flow-compatible catalytic materials that enable modular and continuous biocatalysis [17]. These systems enable efficient cofactor recycling and have been successfully implemented in continuous-flow processes. However, their functionality is inherently limited to enzyme-only systems and thus relies on externally supplied reducing equivalents, preventing internal generation of reducing equivalents from simple gaseous substrates.

Integrating metabolic energy conversion into enzyme-based materials represents a promising yet largely unexplored strategy to overcome this limitation. Here, we introduce gas-powered hybrid catalytic materials that couple cellular metabolism with programmable enzyme networks within a single carrier-free architecture (Figure 1). In this design, metabolically active cells function as internal energy modules that convert gaseous substrates into diffusible intermediates, which are directly linked to enzymatic cofactor regeneration and downstream transformations within the material. Here, "carrier-free" refers specifically to the architecture formed directly from cells and enzymes without an exogenous solid support; optional incorporation into an alginate scaffold results in a carrier-containing composite material that facilitates material recovery and recycling. The resulting hybrid materials spatially confine cells within a percolating enzyme network and are fabricated as monodisperse, ready-to-use beads by a droplet-based cryogenic formulation strategy. Functionally, these materials operate as self-assembled catalytic units that generate biochemical reducing equivalents from gaseous inputs and directly fuel NAD(P)H-dependent reactions, enabling modular coupling to different classes of biocatalysts. By uniting metabolic energy conversion, cofactor regeneration, and programmable enzyme assembly within a single material platform, this work establishes a new class of hybrid catalytic materials for gas-driven biocatalysis.

2 | Results and Discussion

2.1 | Establishing a Gas-Driven Cofactor Regeneration Module

To establish a gas-driven redox module compatible with hybrid catalytic materials, we sought to harness intrinsic metabolic pathways of *E. coli* for hydrogen-driven cofactor regeneration. While native [NiFe]-hydrogenases do not directly reduce $NAD(P)^+$, Hydrogenase 3, a key component of the formate hydrogenlyase (FHL) complex, enables reversible conversion of H_2 and CO_2 to formate [18–21]. This intrinsic pathway provides a direct link between gaseous substrates and soluble redox carriers, thereby

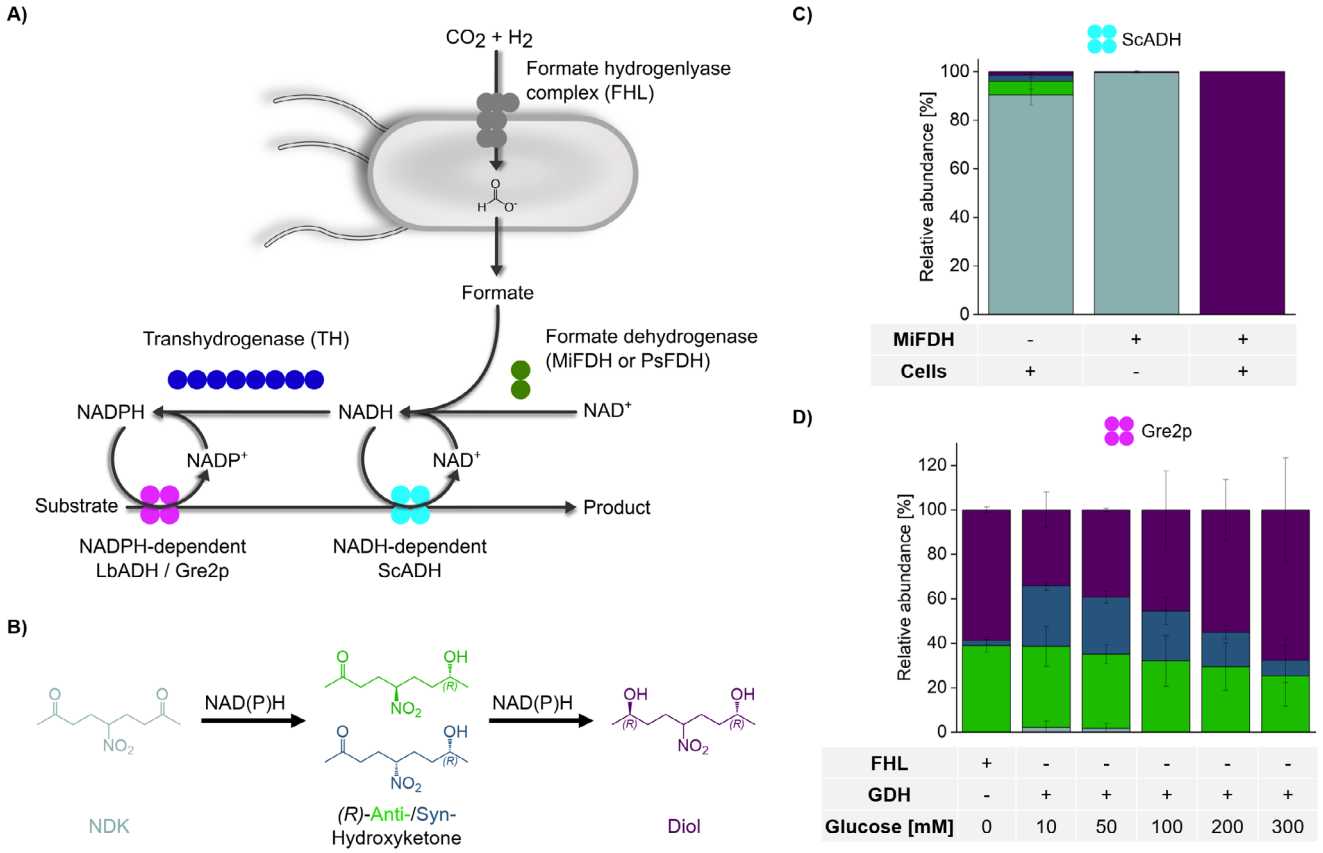

FIGURE 2 | Gas-driven cofactor regeneration as a functional module for hybrid catalytic materials. (A) Concept of the metabolism-based redox module in which the native formate hydrogenlyase (FHL) converts H_2 and CO_2 into formate, which is subsequently oxidized by a formate dehydrogenase (FDH) to generate NADH. Integration of a transhydrogenase enables conversion of NADH into NADPH, thereby expanding the system toward NADPH-dependent biocatalysis. (B) Two-step enzymatic reduction of the prochiral diketone 5-nitrononane-2,8-dione (NDK) to the corresponding diol via hydroxyketone intermediates. (C) Coupling of the FHL-FDH module to the NADH-dependent alcohol dehydrogenase ScADH enables efficient gas-driven reduction of NDK whereas no conversion was observed either in the absence of MiFDH or in the absence of cells, highlighting the necessity of the coupled regeneration module. (D) Coupling to the NADPH-dependent alcohol dehydrogenase Gre2p enables comparison with a glucose dehydrogenase (GDH)-based regeneration system, demonstrating comparable catalytic performance while avoiding sacrificial substrates.

bypassing the need for heterologous hydrogenase expression or external sacrificial substrates.

Crucially, the FHL reaction is reversible, and exposure to H_2 and CO_2 drives formate formation in a pressure-dependent manner. This behavior effectively establishes a metabolic route for hydrogen-driven CO_2 reduction while avoiding the maturation constraints associated with heterologous hydrogenase systems [22], such as those of the soluble hydrogenase from *C. necator*. In contrast to conventional formate production routes, including methanol-based synthesis [23], this intrinsic pathway provides a direct and sustainable route to generate soluble redox equivalents from gaseous substrates, highlighting FHL as an underexplored metabolic module for gas-driven cofactor regeneration.

Based on this concept, we established a closed-loop cofactor regeneration system in which FHL generates formate from H_2 and CO_2, which is subsequently oxidized by a formate dehydrogenase (FDH) to produce NADH (Figure 2A). In this cycle, formate acts as a transient electron carrier linking the metabolic conversion of H_2/CO_2 to enzymatic NADH regeneration, resulting in the net consumption of molecular hydrogen while CO_2 is continuously recycled.

We first optimized the performance of the FHL module under practical conditions. Formate production was quantified under an H_2/CO_2 atmosphere at 0.6 bar overpressure, a pressure regime compatible with standard laboratory equipment. While the dependence of the reaction rate on the H_2/CO_2 ratio was not systematically investigated in this study, the ratio might influence catalytic performance because H_2 is net consumed whereas CO_2 is regenerated within the formate cycle. Thus, increased H_2 availability may favor sustained conversion, provided that sufficient CO_2 remains available for FHL-mediated formate formation. We selected an 80:20 H_2/CO_2 ratio to match gas compositions commonly available in laboratories working with methanogens and acetogens [24, 25], although a 1:1 H_2/CO_2 ratio has also been reported for FHL-mediated formate production [21]. Calculations based on the ideal gas law revealed that approximately 1.2 mmol CO_2 and 4.8 mmol H_2 were initially present in the gas phase. Thus, relative to the 0.025 mmol substrate employed in a standard 5 mL reaction, CO_2 availability is not expected to become limiting under the conditions used in this study. Systematic variation of cell density, storage conditions, and reaction parameters revealed robust formate production across a broad range of conditions (Figure S1). Notably, frozen cell suspensions retained full activity, enabling convenient storage and handling. Under optimized

conditions (OD_{600} = 10, 37 °C, 200 mM Tris buffer), formate concentrations of up to 30 mM were reached within 1 h (Figure S2), while control experiments lacking functional FHL showed no detectable activity, confirming the specificity of the system.

To identify a suitable enzymatic partner for efficient NADH generation, we evaluated several FDHs differing in origin and expected stability (for details on genetic constructs see materials and methods and Tables S1–S3). As a reference, we included the well-characterized PsFDH from *Pseudomonas* sp. 101, which has previously been used for cofactor regeneration [26, 27]. In addition, we investigated a thermophilic FDH from a *Thermoplasmata archaeon* (TaFDH) and a candidate from *Methylacidiphilum infernorum* (MiFDH), selected based on sequence mining [28] and predicted robustness [29]. All enzymes were obtained in high purity, as confirmed by SDS-PAGE analysis (Figure S3). While TaFDH exhibited only low activity in NAD^+ reduction under the tested conditions, both PsFDH and MiFDH showed efficient catalytic performance (Figure S4). Notably, MiFDH displayed markedly enhanced stability, retaining full activity after prolonged incubation and at elevated temperature, whereas PsFDH rapidly lost activity under these conditions.

Direct H_2-driven NAD(P)H regeneration using soluble hydrogenases, such as the NAD-reducing [NiFe]-hydrogenase from *C. necator*, represents an attractive alternative because H_2 oxidation can be coupled directly to cofactor reduction without requiring CO_2/formate cycling or an additional enzyme. However, functional production of these complex metalloenzymes requires dedicated maturation machinery for assembly of the [NiFe]-active site and can result in comparatively low recombinant yields. In contrast, MiFDH can be readily expressed in *E. coli* without additional maturation enzymes and yielded approximately 20 mg L^{-1} culture without process optimization, approximately fourfold higher than reported for the soluble hydrogenase from *C. necator* under comparable laboratory-scale conditions [30, 31]. Thus, while direct hydrogenase-driven NAD(P)H regeneration offers greater catalytic simplicity, the present approach provides practical advantages in terms of enzyme production and accessibility of the biological components.

Coupling of the FHL-MiFDH module to an NADH-dependent alcohol dehydrogenase enabled efficient reduction of the model substrate 5-nitrononane-2,8-dione (NDK), a prochiral diketone frequently used as a model substrate for stereoselective reductions (Figure 2B) [32]. Using the carbonyl reductase from *Streptomyces coelicolor* (ScADH) [33], the FHL-FDH system facilitated the stepwise conversion of NDK to the corresponding hydroxyketones and diol products, thereby demonstrating effective integration of gas-driven cofactor regeneration with downstream asymmetric catalysis (Figure 2C). The system achieved total turnover numbers exceeding 2,200, confirming efficient in situ NADH supply. No conversion was observed either in the absence of MiFDH or in the absence of cells, highlighting the necessity of the coupled regeneration module. Product analysis confirmed the expected stereoselectivity of ScADH (Figure S5), and the overall atom economy reached 82%, substantially exceeding that of glucose-dependent regeneration systems.

Because the selected formate dehydrogenase MiFDH selectively reduces NAD^+ but shows negligible activity toward $NADP^+$ (Figure S6A), an additional enzymatic module was required to enable NADPH-dependent transformations. We therefore introduced the soluble transhydrogenase SthA (TH) from *E. coli*, which catalyzes hydride transfer from NADH to $NADP^+$ and thereby links NADH-based regeneration to NADPH-dependent enzymes. Purified TH displayed the characteristic absorption features of its flavin cofactor FAD, confirming cofactor binding and functional integrity (Figure S7). To further improve performance, key reaction parameters were optimized using a machine-learning-guided approach (SyCoFinder) [34, 35], identifying conditions that enhance NDK conversion under both formate-driven and gas-driven regimes (Figure S8, Table S4).

Under these optimized conditions, incorporation of TH enabled efficient operation of NADPH-dependent alcohol dehydrogenases, including LbADH and Gre2p, thereby extending the cofactor scope of the system (Figure 2D, Figure S8). Benchmarking against a conventional glucose dehydrogenase (GDH)-based regeneration system revealed comparable product formation rates while eliminating the need for sacrificial organic substrates (Figure 2D). Additional experiments using fermentation-derived gas mixtures further confirmed the robustness of the system and its compatibility with alternative gas sources (Figure S8C). Together, these results demonstrate that the FHL-based module provides a versatile platform for cofactor regeneration, combining high catalytic performance with improved atom economy and enabling both NADH- and NADPH-dependent biocatalysis.

2.2 | Intracellular Assembly of Enzyme-Based Hybrid Networks

To enable carrier-free organization of the catalytic enzymes and facilitate their integration into material-based formats, we designed the enzymatic components to self-assemble directly inside the cell. For this purpose, we employed the SpyTag/SpyCatcher (ST/SC) system, which enables spontaneous formation of covalent isopeptide bonds between protein fusion partners [36]. MiFDH was fused to SpyCatcher (SC), while the transhydrogenase SthA (TH) was fused to SpyTag (ST), enabling the formation of covalently linked enzyme networks upon co-expression. Fusion of MiFDH to ST or SC did not impair catalytic activity of the enzymes (Figure S6B). A modular two-plasmid system was established to allow either expression of MiFDH–SC alone or co-expression with TH–ST under arabinose-inducible control. Owing to the octameric nature of TH [37], this design was expected to promote the formation of a three-dimensional protein network resembling an all-enzyme hydrogel (AEH) (Figure 3A).

Intracellular expression of MiFDH-SC was confirmed by SDS-PAGE analysis, showing comparable production levels under different expression conditions (Figure S9A). Covalent assembly of MiFDH-SC and TH-ST was validated both in vitro and in vivo: incubation of purified enzymes resulted in the formation of stable conjugates resistant to denaturation, and bands corresponding to these conjugates were likewise observed in lysates of co-expressing cells (Figure 3B, Figure S9B). Residual unbound TH-ST (lane 5 in Figure 3B) suggests a stoichiometric imbalance, consistent with higher expression levels of TH relative to MiFDH.

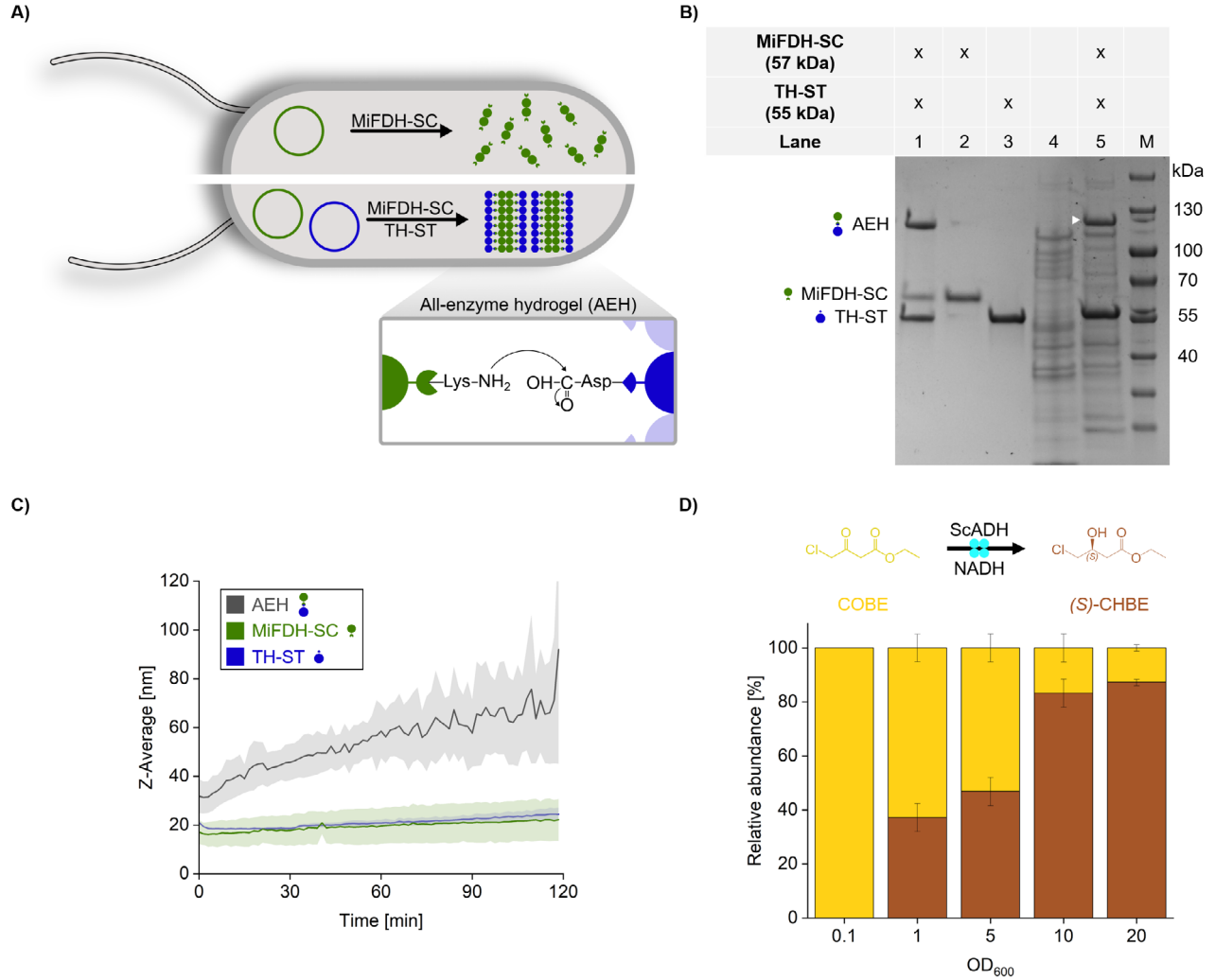

FIGURE 3 | Intracellular assembly and catalytic function of enzyme-based hybrid networks. (A) Schematic representation of intracellular production of MiFDH fused to SpyCatcher (MiFDH–SC) either alone or co-expressed with SpyTag-fused transhydrogenase (TH–ST). Covalent isopeptide bond formation between SpyTag and SpyCatcher (zoom-in) results in the formation of intracellular all-enzyme hydrogel assemblies (AEH). (B) SDS-PAGE analysis confirming formation of covalently linked MiFDH–TH conjugates in co-expressing cells. Lane 1: purified MiFDH–SC and TH–ST incubated for 30 min; lane 2: purified MiFDH–SC; lane 3: purified TH–ST; lane 4: cells without plasmid; lane 5: cells expressing MiFDH/TH AEH. M: protein marker. The arrow indicates the AEH conjugate band. (C) Dynamic light scattering analysis showing nanoscale assembly formation upon mixing of purified MiFDH–SC and TH–ST compared to the individual enzymes. (D) Whole-cell catalysis demonstrating NADH-driven reduction of ethyl 4-chloro-3-oxobutanoate (COBE) with in situ cofactor generation. Error bars in (C) and (D) represent the standard deviation from two independent experiments.

Formation of nanoscale assemblies was further confirmed by dynamic light scattering. While the individual enzymes remained largely monodisperse, mixtures of MiFDH-SC and TH-ST exhibited time-dependent growth of particles reaching hydrodynamic diameters of approximately 75 nm (Figure 3C), consistent with previously reported nanogel dimensions [38, 39].

SDS-PAGE densitometry further revealed intracellular concentrations of approximately 0.5 μM unbound MiFDH-SC and 1.0 μM MiFDH-SC/TH-ST conjugates at OD_{600} = 5 (Figure S9C,D). We next evaluated the functional consequences of intracellular enzyme assembly by quantifying NADH formation under an H_2/CO_2 atmosphere. Cells expressing MiFDH-SC alone or co-expressing MiFDH-SC and TH-ST were compared with cells supplemented with purified MiFDH-SC (Figure S10). After incubation with 2.5 mM NAD^+, cells were removed and NADH formation in the supernatant was quantified fluorometrically.

Supplementation with 4.4 μM MiFDH-SC resulted in nearly complete reduction of the supplied NAD^+, whereas supplementation with 1 μM MiFDH-SC yielded NADH concentrations comparable to those obtained with intracellularly expressed MiFDH-SC. These results indicate that the lower NADH accumulation observed for the intracellular system, in comparison to supplementation with 4.4 μM MiFDH-SC, can largely be attributed to the limited intracellular MiFDH-SC concentration rather than an intrinsic loss of catalytic activity. Nevertheless, externally supplemented MiFDH-SC consistently produced slightly higher NADH levels, likely because FHL-generated formate is released into the extracellular medium [21] and can therefore be directly utilized by the supplemented enzyme. In addition, within the

intracellular environment, both formate and NADH may be consumed by native metabolic processes, thereby competing with the introduced pathway. Co-expression with TH-ST further decreased NADH accumulation, consistent with redistribution of reducing equivalents toward NADPH and subsequent cellular consumption.

Despite these limitations, the intracellularly assembled systems enabled direct whole-cell biocatalysis without the need for protein purification. In combination with the NADH-dependent ScADH, MiFDH-SC-expressing cells achieved near-quantitative conversion of NDK (Figure S11). As expected, no product formation was observed with the NADPH-dependent LbADH in the absence of TH, whereas supplementation with TH restored full activity. The MiFDH/TH co-expression system enabled NADPH-dependent catalysis without external enzyme addition and achieved moderate overall conversion, demonstrating functional integration of NADH generation and NADPH-dependent biocatalysis within a single cellular system. Importantly, covalent assembly of MiFDH-SC and TH-ST into intracellular AEHs did not result in a noticeable loss of catalytic performance compared to cells co-expressing the non-interacting enzyme variants, indicating that enzyme network formation is compatible with efficient cofactor regeneration and downstream catalysis (Figure S11).

Finally, we evaluated the applicability of the system using the industrially relevant β-ketoester ethyl 4-chloro-3-oxobutanoate (COBE), a key precursor for the synthesis of chiral pharmaceutical intermediates. Asymmetric reduction of COBE yields ethyl (S)-4-chloro-3-hydroxybutanoate ((S)-CHBE), an important building block in the synthesis of atorvastatin and related statin drugs [33]. After pre-generation of NADH to avoid substrate inhibition of FDH by the α-haloketone substrate, efficient conversion was achieved, reaching yields above 80% (Figure 3D). Increasing cell density did not further enhance product formation, consistent with a plateau in formate production at higher cell densities (Figure S1A), indicating that formate supply limits further turnover under these conditions. For prolonged operation or higher substrate loadings, continuous H_2 supply may help maintain catalytic performance by preventing depletion of the reducing substrate, as decreasing gas pressure and concomitantly decreasing rates of FHL-mediated formate production have previously been observed during operation in closed reaction vessels [21].

Together, these results demonstrate that intracellular expression of SpyTag/SpyCatcher-functionalized enzymes enables the formation of covalently linked enzyme networks that are catalytically active and can be directly applied as whole-cell biocatalysts. This establishes intracellular self-assembly as a viable route toward hybrid catalytic materials.

2.3 | Cell-Enzyme Hybrid Beads as Programmable Catalytic Materials

To translate intracellular enzyme networks into a practical and application-ready material format, we developed lyophilized cell-enzyme hybrid beads that integrate metabolically active cells with programmable enzyme assemblies within a single particle. The fabrication workflow follows the droplet-based cryogenic formulation strategy outlined in Figure 1B. For bead production, concentrated cell suspensions were combined with purified MiFDH-SC and TH-ST and dispensed as defined droplets (10 μL) into liquid nitrogen, resulting in rapid cryogenic solidification. Subsequent lyophilization yielded mechanically stable, free-flowing beads that can be readily stored, dosed, and rehydrated. Macroscopically, uniform spherical beads with diameters of approximately 1.5 mm were obtained (Figure S12A). Initial attempts to lyophilize cell-based catalytic systems resulted in substantial loss of activity compared to frozen controls (Figure S12B). Incorporation of trehalose as a lyoprotectant restored catalytic performance and enabled the formation of stable and functional hybrid materials.

Environmental scanning electron microscopy (ESEM) provided detailed insight into the internal architecture of the hybrid beads. Beads composed of cells and enzyme components exhibited a highly porous morphology in which cells were embedded within an interconnected enzyme network (Figure 4A–C). Higher-magnification images revealed distinct cellular structures integrated within the surrounding enzyme matrix (Figure 4B,C, red arrows). Incorporation of trehalose during bead preparation induced pronounced structural modulation characterized by the formation of a consolidated outer layer and locally densified regions, suggesting the emergence of a protective matrix that stabilizes the internal architecture (Figure 4D,E). In contrast, control beads composed solely of cells and trehalose lacked this hierarchical organization and instead formed compact agglomerates (Figure 4F), highlighting the critical structural role of the enzyme network in establishing the self-assembled porous hybrid architecture.

The resulting hybrid beads function as programmable catalytic materials that can be directly applied in biotransformations. Catalytic performance scaled linearly with bead number, enabling straightforward adjustment of reaction rates by simple dosing (Figure 4G). Using the NADPH-dependent alcohol dehydrogenase LbADH as a representative downstream catalyst, conversions exceeding 80% were achieved with five beads, corresponding to defined effective concentrations of cells and catalytic enzymes. In this configuration, the embedded MiFDH/TH system acts as a self-contained NADPH-generating module, while the alcohol dehydrogenase is supplied separately. This modular design enables straightforward coupling of the material platform to diverse downstream biocatalysts without modification of the bead composition.

The modular design of the hybrid beads further allows adaptation to different cofactor requirements and catalytic schemes. This versatility was demonstrated using the structurally distinct substrate ethyl 4-chloro-3-oxobutanoate (COBE) in combination with the NADH-dependent alcohol dehydrogenase ScADH (Figure 4H). In contrast to the NADPH-driven NDK system, this setup operates without transhydrogenase and directly utilizes NADH generated by MiFDH. After pre-generation of NADH to mitigate substrate inhibition, efficient conversion was achieved, highlighting the ability to selectively engage different catalytic pathways within the same material platform.

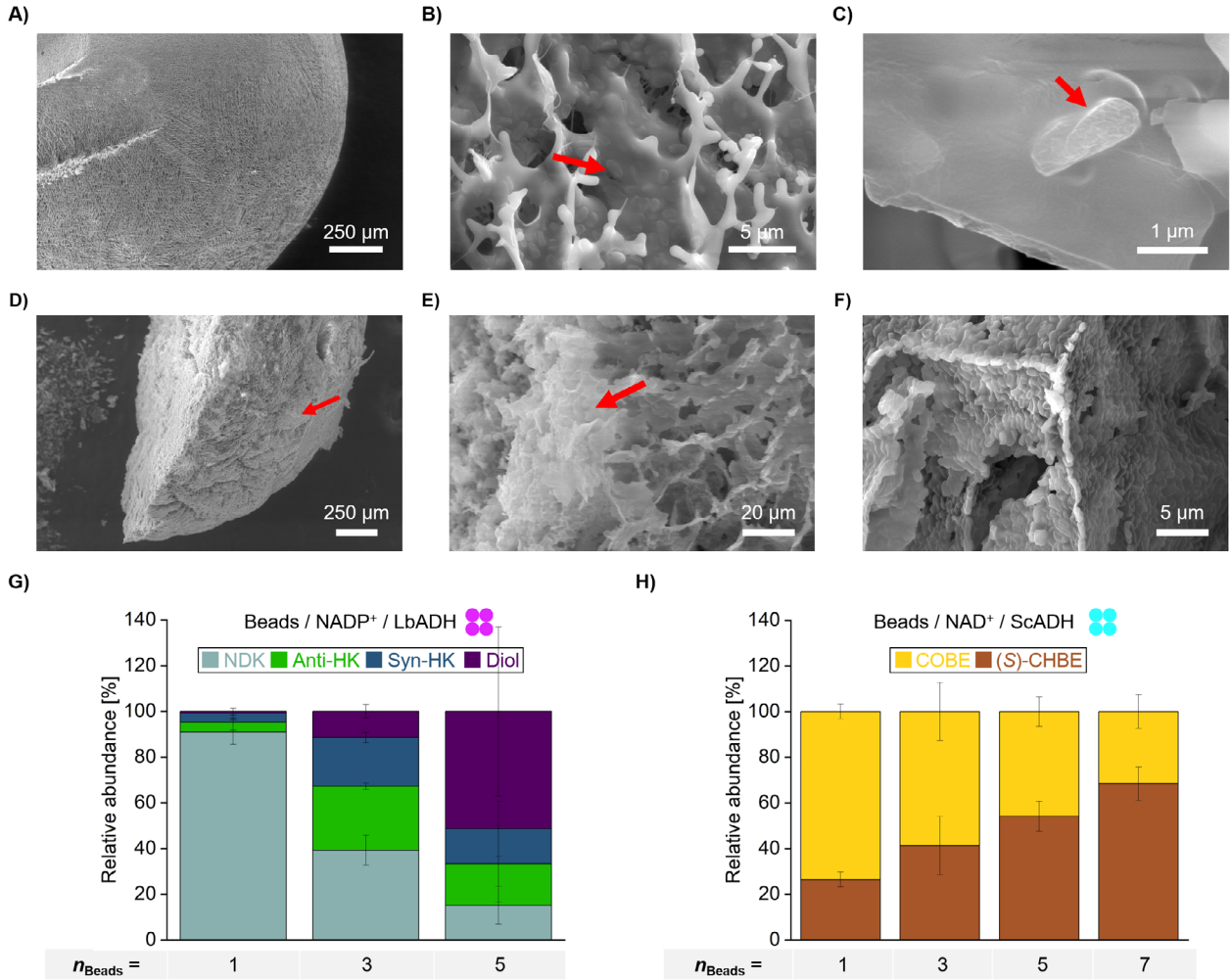

FIGURE 4 | Structural organization and catalytic performance of cell-enzyme hybrid beads. (A–C) Environmental scanning electron microscopy (ESEM) images of hybrid beads composed of cells, MiFDH-SC, and TH-ST without trehalose, revealing a highly porous architecture in which cells are embedded within an interconnected enzyme network. (A) Macroscopic bead morphology. (B, C) Higher-magnification images showing cellular structures integrated within the enzyme matrix (red arrows). (D, E) Beads prepared in the presence of 5% trehalose display pronounced structural modulation characterized by the formation of a consolidated outer layer ("protective shield") and locally densified regions (red arrows). (F) Control beads composed solely of cells and trehalose exhibit an agglomerated, non-porous architecture, highlighting the critical structural role of the enzyme network in establishing the observed porous network. (G) Programmable catalytic activity demonstrated by bead-dosed reduction of NDK using the NADPH-dependent alcohol dehydrogenase LbADH. Reactions were performed in 5 mL volume; one bead corresponds to $OD_{600} \approx 0.4$ and enzyme concentrations of approximately 0.5 µM. (H) Modular catalytic operation demonstrated by reduction of COBE using the NADH-dependent alcohol dehydrogenase ScADH. Cofactors were pre-incubated prior to substrate addition to circumvent substrate inhibition. Error bars in (G) and (H) represent the standard deviation from two independent experiments.

In addition to functional versatility, the hybrid beads remained catalytically active after more than four weeks of dry storage at room temperature (Figure S13A). While the activity decreased by approximately threefold compared to freshly prepared beads (Figure 4G), the residual conversion was comparable to that obtained with freshly prepared trehalose-free formulations (Figure S13B). To further assess the stability of the individual catalytic components, FHL-mediated formate production and MiFDH-SC activity were analyzed separately after prolonged storage (Figure S13C,D). After one week of dry storage at room temperature, the beads retained approximately 47% of the initial formate production and 69% of the initial MiFDH-SC activity. Importantly, beads from the batch previously analyzed after >4 weeks (Figure S13A) still exhibited substantial FHL-mediated formate production and MiFDH-SC activity after a total storage period of five months. These observations underscore the importance of trehalose for preserving catalytic function during lyophilization and prolonged storage. Together, these results establish cell-enzyme hybrid beads as robust, scalable, and programmable catalytic materials that can be configured for diverse redox transformations by simple adjustment of enzyme composition and reaction conditions.

2.4 | Alginate-Encapsulated Hybrid Beads for Enhanced Retention and Recyclability

To extend the hybrid bead concept toward reusable catalytic materials, we introduced an additional encapsulation step using alginate. Cell-enzyme mixtures containing alginate were first

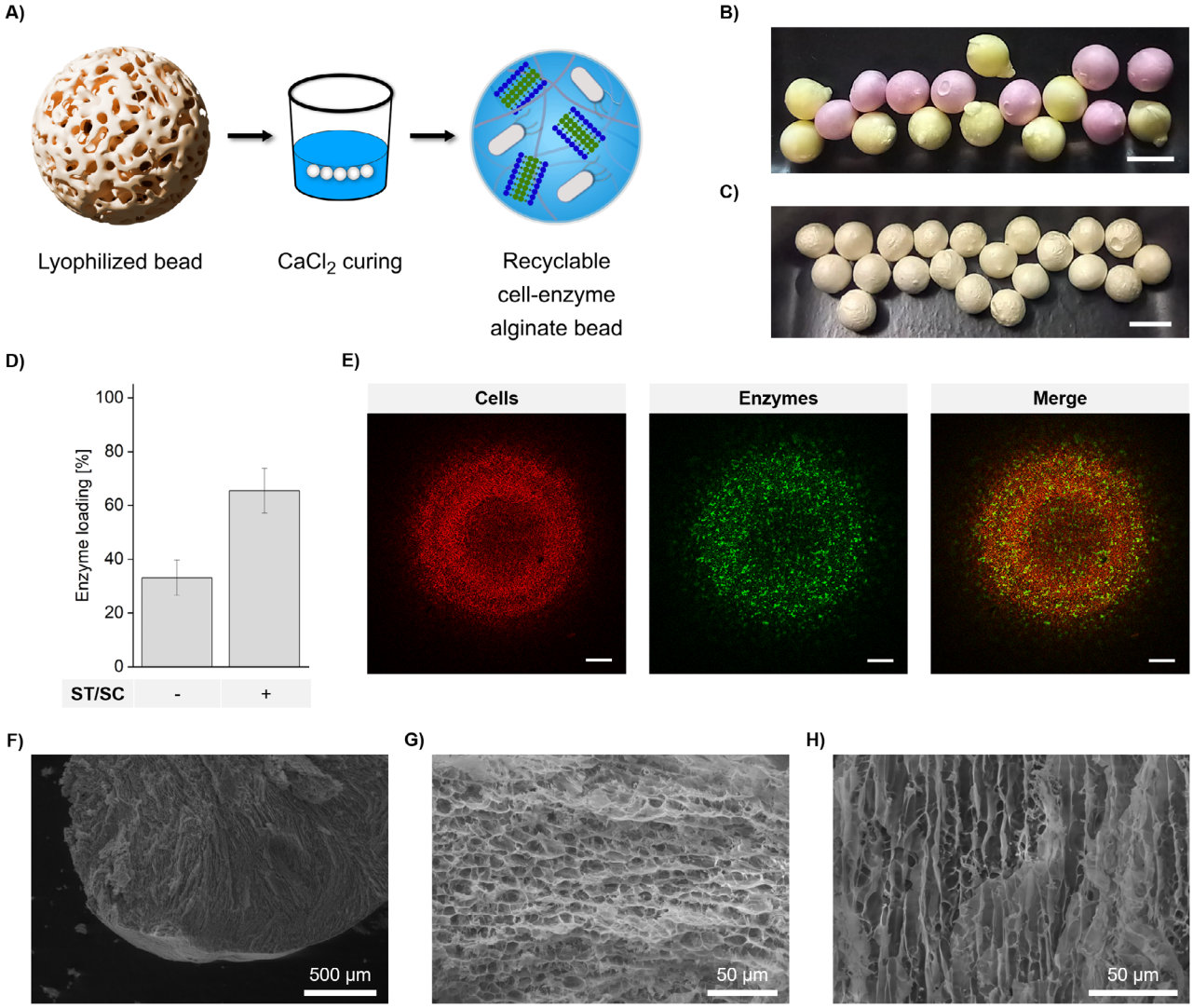

FIGURE 5 | Alginate encapsulation enhances retention, stability, and recyclability of hybrid catalytic beads. (A) Schematic illustration of the encapsulation workflow. Building on the droplet-based fabrication strategy shown in Figure 1B, cell-enzyme mixtures are combined with alginate, processed into lyophilized beads, and subsequently cross-linked in $CaCl_2$ to yield mechanically stabilized composite materials. This modular approach enables the integration of diverse enzymatic and cellular components within the hybrid architecture. (B, C) Representative macroscopic images illustrating the modular composition of alginate-encapsulated beads containing either (B) purified ST-eGFP-ST (yellow) or RFP-expressing *E. coli* (red), and (C) catalytically active assemblies comprising MiFDH-SC, TH-ST, and FHL-expressing *E. coli*. (D) Enzyme retention within alginate beads comparing constructs capable of SpyTag/SpyCatcher-mediated network formation (MiFDH-SC, TH-ST, ST-eGFP-ST) with non-interacting controls (MiFDH, TH, eGFP). Error bars represent the standard deviation from two independent experiments. (E) Laser scanning microscopy images revealing the hierarchical organization of alginate-encapsulated hybrid beads. The central region exhibits reduced fluorescence intensity due to increased optical path length through the bead. Scale bar: 100 µm. (F-H) ESEM micrographs illustrating the morphological impact of alginate encapsulation on hybrid beads. Despite alginate incorporation, the porous morphology with its interconnected structures was retained.

processed via the established cryogenic droplet and lyophilization workflow to yield hybrid beads, which were subsequently soaked in $CaCl_2$ solution to induce cross-linking of the alginate matrix (Figure 5A). This post-fabrication curing step produces mechanically stabilized composite beads while preserving the underlying self-assembled hybrid architecture.

To demonstrate the versatility of this modular design, beads incorporating different functional components were fabricated. Representative macroscopic images confirm the successful integration of either fluorescent reporter systems (purified ST-eGFP-ST or RFP-expressing *E. coli*) or catalytically active assemblies comprising MiFDH-SC, TH-ST, and FHL-expressing *E. coli* (Figure 5B,C). These results illustrate that the alginate encapsulation strategy is compatible with diverse protein and cellular components and enables tailored compositional engineering of the hybrid materials. Importantly, macroscopic inspection confirmed that the beads retained their structural integrity upon cross-linking (Figure S14A).

Because the curing step involves soaking the beads in $CaCl_2$ solution, diffusion of soluble components into the surrounding medium can occur and therefore represents a critical design parameter for the encapsulation strategy. Increasing the Alginate

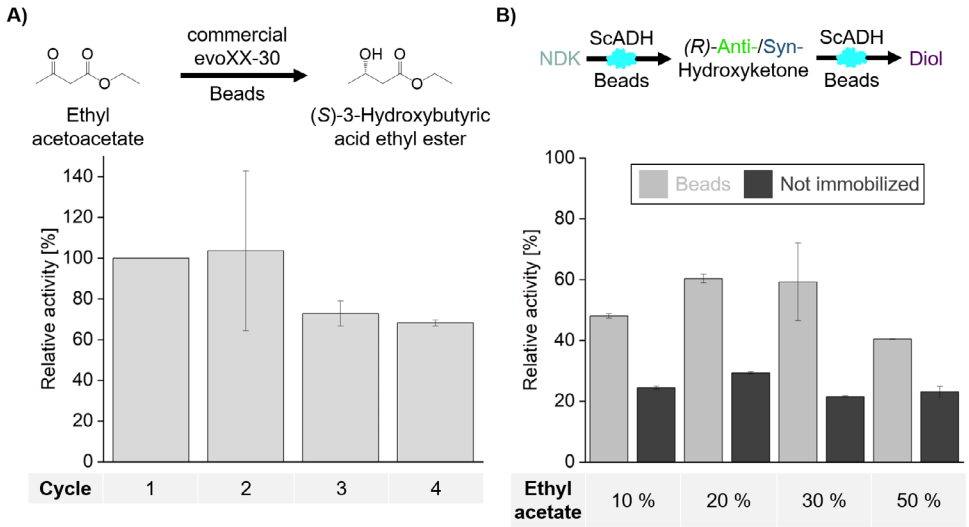

FIGURE 6 | Recyclability and solvent tolerance of alginate-encapsulated hybrid beads. (A) Repeated conversion of ethyl acetoacetate catalyzed by the commercial alcohol dehydrogenase ADH-30 (evoXX), demonstrating sustained catalytic activity and compatibility of the hybrid bead platform with externally supplied biocatalysts. Product formation in the first cycle was normalized to 100%. (B) Stability of immobilized hybrid beads and non-immobilized controls in biphasic ethyl acetate/buffer systems containing increasing amounts of ethyl acetate. Encapsulated materials exhibited enhanced robustness under solvent-containing conditions. NDK conversion in the absence of ethyl acetate was normalized to 100%. Error bars represent the standard deviation from at least two independent experiments.

concentration from 2% to 3% decreased protein diffusion into the supernatant by approximately 35%, as quantified using fluorescent reporter proteins (Figure S14B). To further suppress leakage, we investigated whether covalent network formation via SpyTag/SpyCatcher could restrict diffusion of enzyme components. Beads containing either non-interacting proteins (MiFDH, TH, eGFP) or cross-linkable counterparts (MiFDH-SC, TH-ST, ST-eGFP-ST) were compared. Fluorescence analysis of the supernatant revealed substantial leakage (~70%) for non-cross-linked systems, whereas pre-assembly of an AEH network reduced leakage to below 40% (Figure 5D), demonstrating that covalent enzyme network formation effectively enhances retention within the alginate matrix. To assess retention stability after curing, beads were subjected to sequential wash steps without $CaCl_2$, revealing only negligible release (Figure S14C).

Structural characterization of hybrid beads containing RFP-expressing *E. coli* cells and eGFP-labeled enzyme networks by confocal laser scanning microscopy (CLSM) provided insight into the internal organization of the composite material. Three-dimensional reconstruction of CLSM Z-stacks revealed a homogeneous spatial distribution of both RFP-expressing cells and ST-eGFP-ST-tagged enzyme networks throughout the bead volume, confirming uniform incorporation of cellular and protein-based components within the hybrid architecture (Figure 5E and Figure S15). Ultrastructural analysis by ESEM further revealed a hierarchical organization in which a porous enzyme network is embedded within the surrounding alginate scaffold (Figure 5F–H). Consistent with these observations, gas adsorption measurements confirmed the presence of accessible porosity (Figure S14D), indicating that the composite architecture supports efficient mass transport. Finally, energy-dispersive X-ray spectroscopy verified the expected chemical composition of the cured beads (Table S5).

We next assessed whether encapsulation affects catalytic performance. Activity assays based on NDK conversion revealed only a moderate decrease in activity upon alginate encapsulation, with conversion declining from approximately 60% for non-encapsulated systems to about 45% for encapsulated beads when normalized to enzyme content (Figure S14E). This result indicates that the alginate matrix imposes only minor mass-transfer limitations while largely preserving catalytic function. However, alginate alone was insufficient to protect the catalytic system during drying and rehydration, consistent with previous reports [40]. Incorporation of 5% trehalose during bead preparation proved essential for maintaining catalytic activity. Together, these findings demonstrate that structural confinement and functional stabilization can be decoupled within the material system, with alginate providing mechanical retention and recyclability, while trehalose preserves enzymatic activity during processing and storage.

To assess whether the fabrication procedure preserves cellular functionality, the viability and genetic integrity of encapsulated cells were evaluated. Cells expressing an RFP reporter were cryopreserved at -80 °C for two months, subsequently processed into alginate beads, and released by dissolution of the alginate matrix. Growth assays confirmed selective proliferation consistent with the plasmid-encoded antibiotic resistance profile, while induction with arabinose restored RFP expression, demonstrating preserved plasmid functionality after encapsulation and processing (Figure S16). Notably, no viable cells were recovered from formulations lacking trehalose, confirming the critical role of trehalose for maintaining cellular integrity during bead fabrication.

The resulting composite beads enable efficient catalyst recovery and reuse (Figure 6). Using a commercial alcohol dehydrogenase

(ADH-30, evoXX) [41, 42], repeated conversion of ethyl acetoacetate was achieved over multiple cycles, demonstrating sustained catalytic performance and compatibility with commercial enzymes (Figure 6A). Given the known tolerance of ScADH to organic solvents and the relevance of ethyl acetate for product extraction [33, 43], the stability of encapsulated materials in a biphasic ethyl acetate/buffer system was also investigated. While non-immobilized components achieved higher NDK conversion under solvent-free conditions (Figure S17), the immobilized beads proved markedly more robust in the presence of ethyl acetate (Figure 6B), confirming their suitability for demanding reaction environments.

Together, these results establish alginate encapsulation as an effective strategy to transform cell-enzyme hybrid beads into reusable, structurally stabilized catalytic materials with reduced leaching, preserved activity, and enhanced robustness. Combined with the intrinsic modularity of the underlying enzyme network, this approach enables the design of adaptable catalytic systems for diverse reaction environments.

3 | Conclusions

In summary, we establish cell-enzyme hybrid materials that integrate cellular metabolism with programmable enzyme networks to enable gas-powered biocatalysis. By leveraging the native formate hydrogenlyase (FHL) machinery of *E. coli*, gaseous substrates (H_2 and CO_2) are directly converted into reducing equivalents that fuel downstream enzymatic transformations. Coupling to a highly stable formate dehydrogenase (MiFDH) and a soluble transhydrogenase (TH) enables flexible access to both NADH- and NADPH-dependent reaction pathways, providing a modular redox platform that can be readily adapted to diverse catalytic requirements.

A key advance of this work is the translation of these catalytic systems into defined material formats. Lyophilized hybrid beads and their alginate-encapsulated counterparts constitute programmable, ready-to-use catalytic materials that combine structural organization, cofactor regeneration, and catalytic function within a single entity. The homogeneous spatial organization of cells and enzyme networks within the composite structure further suggests that diffusion pathways and catalytic sites are distributed throughout the bead interior, enabling efficient coupling of metabolic energy conversion and enzymatic catalysis within the material. The resulting "count-and-add" workflow allows straightforward implementation without complex process control, while maintaining high catalytic performance and enabling catalyst recycling and operation under non-conventional conditions.

Compared to existing hydrogen-driven systems based on heterologous hydrogenases [31, 44], this approach circumvents the need for complex enzyme maturation and specialized host organisms by exploiting endogenous metabolic pathways. At the same time, the gas-fed regeneration strategy offers improved atom economy and avoids accumulation of organic by-products associated with conventional sacrificial substrates, providing a conceptually simple alternative for redox biocatalysis.

Beyond the specific reactions demonstrated here, the combination of metabolic energy conversion, programmable enzyme assembly, and materials engineering defines a generalizable strategy for the design of adaptive catalytic systems. By bridging the gap between biological complexity and practical usability, gas-powered hybrid catalytic materials provide a foundation for scalable and user-defined biomanufacturing processes.

Acknowledgements

This work was supported through the Helmholtz Association program "Materials Systems Engineering" under the topic "Adaptive and Bioinstructive Materials Systems" (Funding code: 43.33.11). We gratefully acknowledge Sarah Gliemann, Farina Witt and Maria Alessandra Martini for their support in protein production. We sincerely thank Gary Sawers and Frank Sargent for providing the *E. coli* strains and Andrea Weckbecker (evoXX) for providing the alcohol dehydrogenases. In addition, we thank Dr. Alexei Kiselev, Dr. Yue Meng and Simone Weigel for experimental help.

Open access funding enabled and organized by Projekt DEAL.

Funding

This work was supported through the Helmholtz Association Program "Materials Systems Engineering" under the topic "Adaptive and Bioinstructive Materials Systems" (Funding code: 43.33.11).

Conflicts of Interest

M.S., K.S.R., and C.M.N. are inventors on a patent application related to the technology described in this work.

Data Availability Statement

The data of this study are available from the corresponding author upon reasonable request.

References

1. R. A. Sheldon and J. M. Woodley, "Role of Biocatalysis in Sustainable Chemistry," *Chemical Reviews* 118 (2018): 801–838.

2. B. Hauer, "Embracing Nature's Catalysts: A Viewpoint on the Future of Biocatalysis," *ACS Catalysis* 10 (2020): 8418–8427.

3. E. L. Bell, W. Finnigan, S. P. France, et al., "Biocatalysis," *Nature Reviews Methods Primers* 1 (2021): 46.

4. S. Wu, R. Snajdrova, J. C. Moore, K. Baldenius, and U. T. Bornscheuer, "Biocatalysis: Enzymatic Synthesis for Industrial Applications," *Angewandte Chemie International Edition* 60 (2021): 88.

5. R. Buller, S. Lutz, R. J. Kazlauskas, R. Snajdrova, J. C. Moore, and U. T. Bornscheuer, "From Nature to Industry: Harnessing Enzymes for Biocatalysis," *Science* 382 (2023): adh8615.

6. L. S. Vidal, C. L. Kelly, P. M. Mordaka, and J. T. Heap, "Review of NAD(P)H-Dependent Oxidoreductases: Properties, Engineering and Application," *Biochimica et Biophysica Acta (BBA)—Proteins and Proteomics* 1866 (2018): 327–347.

7. S. Mordhorst and J. N. Andexer, "Round, Round We Go—Strategies for Enzymatic Cofactor Regeneration," *Natural Product Reports* 37 (2020): 1316–1333.

8. A. Al-Shameri, S. J. P. Willot, C. E. Paul, F. Hollmann, and L. Lauterbach, "H_2 as a Fuel for Flavin- and H_2O_2-Dependent Biocatalytic Reactions," *Chemical Communications* 56 (2020): 9667–9670.

9. J. Preissler, H. A. Reeve, T. Zhu, et al., "Dihydrogen-Driven NADPH Recycling in Imine Reduction and P450-Catalyzed Oxidations Mediated

by an Engineered O_2 -Tolerant Hydrogenase," *Chemcatchem* 12 (2020): 4853–4861.

10. M. Weldon and C. Euler, "Physiology-Informed Use of Cupriavidus Necator in Biomanufacturing: A Review of Advances and Challenges," *Microbial Cell Factories* 24 (2025): 30.

11. K. S. Rabe, J. Muller, M. Skoupi, and C. M. Niemeyer, "Cascades in Compartments: En Route to Machine-Assisted Biotechnology," *Angewandte Chemie International Edition* 56 (2017): 13574–13589.

12. S. P. France, L. J. Hepworth, N. J. Turner, and S. L. Flitsch, "Constructing Biocatalytic Cascades: In Vitro and In Vivo Approaches to de Novo Multi-Enzyme Pathways," *ACS Catalysis* 7 (2017): 710–724.

13. J. M. Sperl and V. Sieber, "Multienzyme Cascade Reactions—Status and Recent Advances," *ACS Catalysis* 8 (2018): 2385–2396.

14. J. M. Woodley, "Accelerating the Implementation of Biocatalysis in Industry," *Applied Microbiology and Biotechnology* 103 (2019): 4733–4739.

15. J. Nazor, J. Liu, and G. Huisman, "Enzyme Evolution for Industrial Biocatalytic Cascades," *Current Opinion in Biotechnology* 69 (2021): 182–190.

16. S. P. Stalter, K. S. Rabe, and C. M. Niemeyer, "Carrier-Free Enzyme Immobilization for High-Density Catalytic Architectures in Flow Biocatalysis," *JACS Au* 6 (2026): 1411–1423.

17. J. Kühne, J. S. Hertel, A. Delavault, et al. Programmable Carrier-Free All-Enzyme Beads for Modular Continuous-Flow Biocatalysis. Karlsruhe Institute of Technology (KIT). https://doi.org/10.35097/9e4a508tu9xaud33.

18. J. S. McDowall, B. J. Murphy, M. Haumann, T. Palmer, F. A. Armstrong, and F. Sargent, "Bacterial Formate Hydrogenlyase Complex," *Proceedings of the National Academy of Sciences* 111 (2014): E3948.

19. R. Steinhilper, G. Höff, J. Heider, and B. J. Murphy, "Structure of the Membrane-Bound Formate Hydrogenlyase Complex From Escherichia Coli," *Nature Communications* 13 (2022): 5395.

20. M. Roger, C. P. Reed Thomas, and F. Sargent, "Harnessing Escherichia coli for Bio-Based Production of Formate under Pressurized H_2 and CO_2 Gases," *Applied and Environmental Microbiology* 87 (2021): 00299.

21. M. Roger, F. Brown, W. Gabrielli, and F. Sargent, "Efficient Hydrogen-Dependent Carbon Dioxide Reduction by Escherichia coli," *Current Biology* 28 (2018): 140–145.e2.

22. F. Leo, F. M. Schwarz, K. Schuchmann, and V. Müller, "Capture of Carbon Dioxide and Hydrogen by Engineered Escherichia coli: Hydrogen-Dependent CO_2 Reduction to Formate," *Applied Microbiology and Biotechnology* 105 (2021): 5861–5872.

23. F. Meng, Z. Shen, X. Lin, et al., "Industrially Viable Formate Production with 50% Lower CO_2 Emissions," *Energy & Environmental Science* 18 (2025): 3680–3688.

24. E. Gak, M. Tyurin, and M. Kiriukhin, "Genome Tailoring Powered Production of Isobutanol in Continuous CO_2/H_2 Blend Fermentation Using Engineered Acetogen Biocatalyst," *Journal of Industrial Microbiology and Biotechnology* 41 (2014): 763–781.

25. M. Szuhaj, B. Kakuk, R. Wirth, G. Rákhely, K. L. Kovács, and Z. Bagi, "Regulation of the Methanogenesis Pathways by Hydrogen at Transcriptomic Level in Time," *Applied Microbiology and Biotechnology* 107 (2023): 6315–6324.

26. A. M. Rojkova, A. G. Galkin, L. B. Kulakova, et al., "Bacterial Formate Dehydrogenase. Increasing the Enzyme Thermal Stability by Hydrophobization of Alpha-Helices," *FEBS Letters* 445 (1999): 183–188.

27. A. A. Pometun, S. Y. Kleymenov, S. A. Zarubina, et al., "Comparison of Thermal Stability of New Formate Dehydrogenases by Differential Scanning Calorimetry," *Moscow University Chemistry Bulletin* 73 (2018): 80–84.

28. J. Hon, S. Borko, J. Stourac, et al., "EnzymeMiner: Automated Mining of Soluble Enzymes with Diverse Structures, Catalytic Properties and Stabilities," *Nucleic Acids Research* 48 (2020): W104–W109.

29. J. Hei Derek and S. C. Douglas, "Pressure Stabilization of Proteins from Extreme Thermophiles," *Applied and Environmental Microbiology* 60 (1994): 932–939.

30. D. L. Siebert, F. Sargent, A. Al-Shameri, and V. Sieber, "Development of a Universal Platform for the Heterologous Expression of Bidirectional [Ni–Fe]-Hydrogenases," *ACS Synthetic Biology* 14 (2025): 2710.

31. J. Schiffels, O. Pinkenburg, M. Schelden, E.-H. A. A. Aboulnaga, M. E. M. Baumann, and T. Selmer, "An Innovative Cloning Platform Enables Large-Scale Production and Maturation of an Oxygen-Tolerant [NiFe]-Hydrogenase from Cupriavidus Necator in Escherichia coli," *PLoS ONE* 8 (2013): 68812.

32. J. S. Hertel, M. A. Martini, M. Stoeckle, A. J. Weber, K. S. Rabe, and C. M. Niemeyer, "Harnessing Non-Covalent Protein–Protein Interaction Domains for Production of Biocatalytic Materials Systems," *Advanced Functional Materials* 35 (2025): 13931.

33. M. Li, Z.-J. Zhang, X.-D. Kong, H.-L. Yu, J. Zhou, and J.-H. Xu, "Engineering Streptomyces Coelicolor Carbonyl Reductase for Efficient Atorvastatin Precursor Synthesis. Applied and Environmental Microbiology," *Applied and environmental microbiology* 83 (2017): 00603.

34. S. M. Moosavi, A. Chidambaram, L. Talirz, M. Haranczyk, K. C. Stylianou, and B. Smit, "Capturing Chemical Intuition in Synthesis of Metal-Organic Frameworks," *Nature Communications* 10 (2019): 539.

35. L. Pilz, M. Koenig, M. Schwotzer, H. Gliemann, C. Wöll, and M. Tsotsalas, "Enhancing the Quality of MOF Thin Films for Device Integration Through Machine Learning: A Case Study on HKUST-1 SURMOF Optimization," *Advanced Functional Materials* 34 (2024): 2404631.

36. B. Zakeri, J. O. Fierer, E. Celik, et al., "Peptide Tag Forming a Rapid Covalent Bond to a Protein, Through Engineering a Bacterial Adhesin," *Proceedings of the National Academy of Sciences* 109 (2012): E690.

37. M. Partipilo, G. Yang, M. L. Mascotti, H. J. Wijma, D. J. Slotboom, and M. W. Fraaije, "A Conserved Sequence Motif in the Escherichia coli Soluble FAD-Containing Pyridine Nucleotide Transhydrogenase is Important for Reaction Efficiency," *Journal of Biological Chemistry* 298 (2022): 102304.

38. T. Peschke, P. Bitterwolf, S. Gallus, et al., "Self-Assembling All-Enzyme Hydrogels for Flow Biocatalysis," *Angewandte Chemie International Edition* 57 (2018): 17028–17032.

39. M. Stoeckle, C. M. Domínguez, A. Hanes, et al., "A Carbonic Anhydrase-Based Nanogel for Cyanobacterial Growth Enhancement," *Materials Today Bio* 35 (2025): 102622.

40. M. V. Traffano-Schiffo, M. Castro-Giraldez, P. J. Fito, and P. R. Santagapita, "Encapsulation of Lactase in Ca(II)-Alginate Beads: Effect of Stabilizers and Drying Methods," *Food Research International* 100 (2017): 296–303.

41. D. Colombo, E. Brenna, F. G. Gatti, et al., "Chemoselective Biohydrogenation of Alkenes in the Presence of Alkynes for the Homologation of 2-Alkynals/3-Alkyn-2-ones into 4-Alkynals/Alkynols," *Advanced Synthesis & Catalysis* 361 (2019): 2638–2648.

42. A. Artasensi, I. Bassanini, E. E. Ferrandi, et al., "Chemoenzymatic Approach Towards the Synthesis of the Antitumor and Antileishmanial Marine Metabolite (+)-Harzialactone a Via the Stereoselective, Biocatalyzed Reduction of a Prochiral Ketone," *Bioorganic Chemistry* 138 (2023): 106675.

43. L.-J. Wang, C.-X. Li, Y. Ni, J. Zhang, X. Liu, and J.-H. Xu, "Highly Efficient Synthesis of Chiral Alcohols With A Novel NADH-Dependent Reductase From Streptomyces Coelicolor," *Bioresource Technology* 102 (2011): 7023–7028.

44. R. L. Bertrand, J. Panich, A. E. Cowan, et al., "Feedstock-Efficient Conversion Through Hydrogen and Formate-Driven Metabolism in Escherichia Coli," *Metabolic Engineering* 93 (2026): 194–207.

Supporting Information

Additional supporting information can be found online in the Supporting Information section.

Supporting File: adfm78174-sup-0001-SuppMat.pdf.